

Investigation of the Role of Crown Crack in Cohesive Soil Slope and Its Effect on Slope Stability Based on Extended Finite Element Method

Yiding Bao (✉ baoyd17@mails.jlu.edu.cn)

Institute of Mountain Hazards and Environment

Yuchao Li

Jilin University

Yansong Zhang

Jilin University

Jianhua Yan

Jilin University

Xin Zhou

Chongqing Jiaotong University

Research Article

Keywords: XFEM, stability analysis, crown crack, crack propagation, stress status

Posted Date: May 18th, 2021

DOI: <https://doi.org/10.21203/rs.3.rs-529550/v1>

License:   This work is licensed under a Creative Commons Attribution 4.0 International License.

[Read Full License](#)

Version of Record: A version of this preprint was published at Natural Hazards on July 30th, 2021. See the published version at <https://doi.org/10.1007/s11069-021-04947-8>.

1 **Investigation of the role of crown crack in cohesive soil slope and its effect on slope stability based on**
2 **extended finite element method**

3 Yiding Bao^{1,2*} · Yuchao Li^{2*} · Yansong Zhang² · Jianhua Yan² · Xin Zhou³

4 ¹ Key Laboratory of Mountain Hazards and Earth Surface Process / Institute of Mountain
5 Hazards and Environment, Chinese Academy of Sciences (CAS), No. 9, Block 4, South Renmin
6 Road, Chengdu 610041, China

7 ² College of Construction Engineering, Jilin University, Changchun, 130026, China

8 ³ School of River and Ocean Engineering, Chongqing Jiaotong University, 400074 Chongqing,
9 China

10 * Corresponding author. Tel.: +86 18204315366

11 * Email address: baoyd17@mails.jlu.edu.cn / baoyd@imde.ac.cn

12 **Abstract**

13 Tensile cracks in soil slopes, especially developing at the crown, have been increasingly recognized as the
14 signal of slope metastability. In this paper, the role of crown cracks in natural soil slopes was investigated and
15 their effect on stability was studied. A numerical slope model based on the extended finite element method
16 (XFEM) simulating the tensile behavior of soil was used. Before the simulation, a numerical soil tensile test
17 was applied to validate the use of XFEM on tensile behavior of soil. Slope failure was simulated by using
18 strength reduction technique, which can determine the potential slip surface of slope. The simulation results
19 show that the crown crack forms in natural soil slopes when the plastic zone starts penetrating, and therefore it
20 is reasonable to consider the crown crack as the signal of slope metastability. A sensitivity analysis shows that
21 cracks are at the position of the tension zone or very long can obviously affect the slope stability. The stress
22 variation analysis from the initial deformation to slip surface penetration shows that the slope is at a state of
23 compressive stress initially. When plastic zone starts to penetrate, the upper part of slope generates tension zone,
24 but the extent of tension zone is limited until slope failure. This shows why tensile cracks are difficult to form

25 and be stretched in the deep part of the slope. The application of XFEM on slope stability analysis can be used
26 to assess the tensile strength of soil and predict slope failure disaster.

27 **Keywords:** XFEM, stability analysis, crown crack, crack propagation, stress status

28 **Introduction**

29 Landslides are one of the most common geological disasters in nature. Many catastrophic landslides occur
30 all over the world each year, causing loss of property and life (Tang et al., 2009; Yin et al., 2016; Gianvito et
31 al., 2018; Chen et al., 2018b; Zhang et al., 2019a;). Landslide is a form of mass movement, including diverse
32 ground movements such as fall, topple, slide, spread, and flow (Hungur et al., 2014). All these types of ground
33 movements exhibit mass separation behavior, generating cracks before mass separation. Some landslide events
34 has exhibited the whole process of failure (Fan et al., 2018; Ouyang et al., 2019; Chen et al., 2019), and one
35 typical case is the Baige landslide. Researchers applied remote-sensing images and InSAR to the Baige landslide,
36 to analyze its historical deformation (Xu et al., 2018; Ouyang et al., 2019). They found deformation firstly
37 occurred at the front part of the slope at the initial stage of the deformation; then as time goes on, large-scale
38 tensile cracks and drop heads formed at the slope crown; finally, with deformation developing, a slide occurred.
39 The case shows a common failure process of landslides. Although, many landslide events (Steiakakis et al.,
40 2009; Chen et al., 2018a; Tang et al., 2019; Fan et al., 2019) and field investigations (Fig.1) have proven that
41 crown cracks are the signal of slope metastability during the long-term slow deformation process, there are still
42 some issues deserve researching, such as at what stage of slope deformation will the crown cracks form? How
43 do these cracks form? What's the maximum length the crack can be? Do these cracks affect the slope stability?
44 Although landslide laboratory tests have been carried out to answer some of them (Tang et al., 2019), some data
45 cannot be easily acquired from the laboratory tests, limiting exploring these questions. Questions such as why

46 the depth of a crack cannot develop downward without limitation are still unexplained. Knowing the answer of
47 these questions is important for comprehending landslide behavior as well as the landslide prevention.

48 Numerical simulation can help researchers obtain extra data, which is not available in laboratory tests.
49 Nowadays, the most common methods to evaluate slope stability with cracks are the limit equilibrium method
50 (LEM) (Bishop 1973; Seed et al., 1990; Koerner and Soon, 2000) and finite element method (FEM) (Griffiths
51 and Lane., 1999; Qu et al., 2009; Bao et al., 2019; Lei et al., 2021). In addition, some new methods such as
52 discrete element method (DEM) (Zhou et al., 2009; Bao et al., 2020), smoothed particle hydrodynamics (SPH)
53 (Li et al., 2019; Ray et al., 2019), and material point method (MPM) (Liu et al., 2019; Conte et al., 2019) have
54 been developed for analyzing slope stability as well as the post-failure movement. The analysis of slope stability
55 using these new methods mainly depends on the strength reduction technique, and they have advantages for the
56 analysis of large-deformation issues. However, these methods still have some limitations in stability analysis.
57 In the DEM, the behavior of the material depends on the interactions between particles. It's difficult to measure
58 some of microscopic parameters between particles, and there is no strong theory to illustrate relationship
59 between the magnitude of macroscopic and microscopic parameters. Thus, it is very time-consuming to
60 determine proper parameters, especially in the strength reduction progress. The SPH and MPM are also time-
61 consuming compared to LEM and FEM. The computation accuracy of SPH as well as MPM is lower than FEM
62 in the small deformation process before slope failure. And although these new methods can be used for slope
63 stability analysis in theory, they lack large amounts of engineering validation compared to LEM and FEM,
64 especially in the case involving cracks. As for the LEM, it is a classical method which has been used for the
65 slope stability analysis involving cracks (Michalowski 2012; Michalowski 2013; Tang et al., 2019). However,
66 there are many limitations in the LEM to analyze a problem with cracks. Cracks in the LEM can only be used
67 for the calculation of factor of safety (FOS). Cracks need to be pre-set in the model, and cannot be updated with

68 calculations. And slope deformation cannot be shown in the LEM. FEM can overcome these shortcomings in
69 the LEM, which makes it a better choose for slope stability analysis involving cracks.

70 The conventional FEM (CFEM) is difficult to be used to simulate discontinuous elements such as cracks
71 due to meshing limitation. To overcome the shortcomings of CFEM in the discontinuous analysis, some theories
72 including the efficient remeshing techniques (Areias et al., 2013; 2015), the numerical manifold method (Shi
73 1991; Ma et al., 2009), and the extended FEM (XFEM) (Moës et al., 1999) are proposed. Most of the methods
74 modelling crack propagation by FEM heavily depend on the mesh alignment (Rabczuk and Ren, 2017), but the
75 XFEM can avoid the problem. In XFEM, special functions and element segmentation method are used to fuse
76 to solve the solution of finite element approximation. And the level set method is used to show the geometry
77 and extension process of the discontinuous interface. Different from the CFEM, XFEM no longer has strict
78 requirements on the accuracy and repetition of the network, and has no specific restrictions on the crack front
79 and growth path. And XFEM has high computational efficiency. Therefore, this method has been widely applied
80 in fracture mechanics and engineering (Sanborn and Jean H, 2011; Wang et al., 2015; Zhou and Chen, 2019).

81 In this study, to investigate the role of crown cracks in soil slope, XFEM based on ABAQUS software was
82 used for the simulation of tensile behavior in soil. The authors set a series of numerical simulation to explore
83 the formation of crown cracks and the effect of a tensile crack on soil slope stability. Factors, including the
84 position, strength, and depth of cracks were considered for sensitivity analysis, and combined with stress
85 analysis, some interesting phenomena were found with conclusions made.

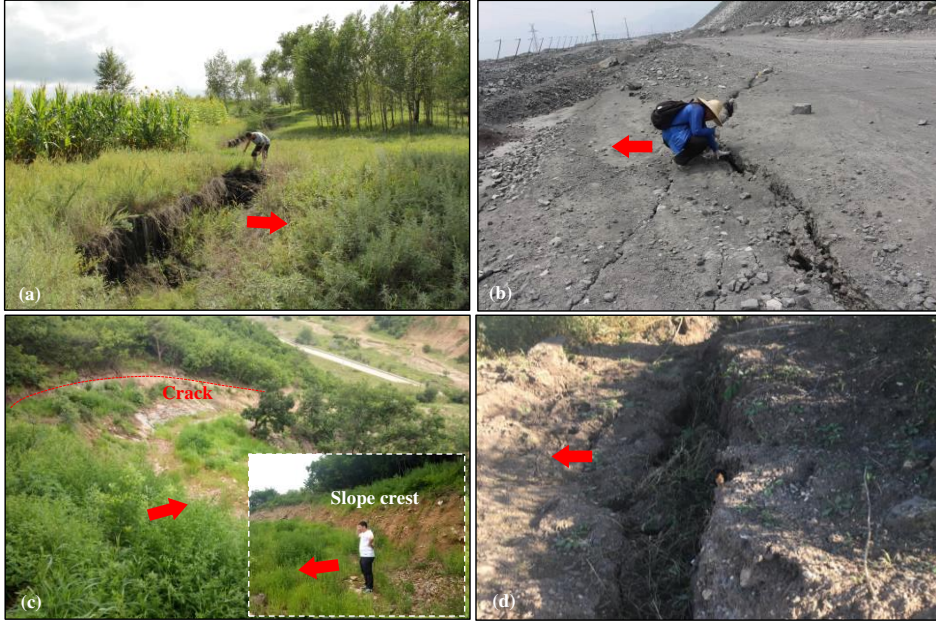


Fig. 1. Crown cracks appear in some soil slopes. (a) A potential landslide with obvious deformation in Jilin province in 2016, (b) a potential landslide in a waste dump in Sichuan province in 2016, (c) a potential landslide with obvious deformation in Jilin province in 2015, and (d) a potential landslide in Liaoning province in 2019. Red Arrows denote to the direction of slides.

86

87 Methodology

88 XFEM

89 The extended element method (XFEM) is an improvement on FEM for the research of discontinuous
 90 processes, such as cracks. It is proposed by the Ted Belytschko team (Moës et al., 1999). In the XFEM, a special
 91 enrichment function is used for the discontinuity. When the enrichment function is applied to crack analysis, it
 92 can well fit the asymptotic function of the tip, and has a good expression for the displacement jump on the crack
 93 surface. The standard extended finite element approximate equivalent equation of u function in ABAQUS:

$$94 \quad \sum_{I=1}^N N_I(x)[u_I + H(x)a_I + \sum_{\alpha=1}^4 F_{\alpha}(x)b_I^{\alpha}] \quad (1)$$

95 In equation (1), $N_I(x)$ is the normal shape function of the node. The first term on the right of the equal
 96 sign is available for all nodes, and it is related to the continuous part of finite element. The definition of u_I is
 97 the displacement vector of the normal node. The second term applies to particular nodes, such as a shape

98 function that supports a node cut inside a crack. The term is the product of nodal enriched degree of freedom
 99 vector a_I , and $H(x)$ denotes to the jump function across the discontinuous interface. The third term is the most
 100 limited, only for the shape function supporting the node cut off by the crack tip. The term is the product of nodal
 101 enriched degree of freedom vector b_I^α . $F_\alpha(x)$ describes the elastic asymptotic properties of the crack tip. The
 102 jump function $H(x)$ is described as follows.

$$103 \quad H(x) = \begin{cases} 1 & \text{if } (x - x^*) \cdot n \geq 0, \\ -1 & \text{otherwise} \end{cases} \quad (2)$$

104 Where, x represents the sampling point; x^* represents the point with the shortest distance from x on the crack;
 105 n represents the unit vector of the crack outward normal at x^* .

106 Fig. 2a shows the asymptotic function of crack tip in isotropic elastic material, and the formula is:

$$107 \quad F_\alpha(x) = [\sqrt{r} \sin \frac{\theta}{2}, \sqrt{r} \cos \frac{\theta}{2}, \sqrt{r} \sin \theta \sin \frac{\theta}{2}, \sqrt{r} \sin \theta \cos \frac{\theta}{2}] \quad (3)$$

108 In equation (3), (r, θ) is polar coordinate representation, whose physical meaning is that the origin is at the
 109 crack tip.

110 The node subset I^* is the set of all nodes of elements cut by discontinuities. The global enrichment
 111 function can only work in those elements whose nodes are all in the subset, I^* . The level set function is a scalar
 112 function whose zero-level represents discontinuity. The level-set function $\phi(x)$ which is described as follows
 113 determines whether an element is cut by discontinuities.

$$114 \quad \text{cut element: } \min(\phi_i) \max(\phi_i) < 0 \quad (i \in I^{el}) \quad (4)$$

$$115 \quad \text{uncut element: } \min(\phi_i) \max(\phi_i) > 0 \quad (i \in I^{el}) \quad (5)$$

$$116 \quad \phi(x) = \pm \min_{x_\Gamma \in \Gamma} \|x - x_\Gamma\|, \quad \forall x \in \Omega \quad (6)$$

117 In the above equation I^{el} represents the set of element nodes.

118 The domain Ω is divided by the discontinuity into Ω_p^+ and Ω_p^- , and the level set function can be positive
 119 or negative on either side of the discontinuity, respectively. In the domain Ω , the phantom node is used to

120 describe the cracked behavior, and the node is initially superimposed on the real node before element separation.
 121 When there is no crack in elements, the phantom node corresponds to real nodes with completely constraint. If
 122 the element is divided by the discontinuity into two parts, corresponding phantom nodes and real nodes will
 123 separate, and no longer be tied together (Fig.2b). They are then interpolated by standard finite element shape
 124 functions:

$$\phi^h(x) = \sum_{i \in I} N_i(x) \cdot \phi_i \quad (7)$$

126 where h is the number of interpolated elements.

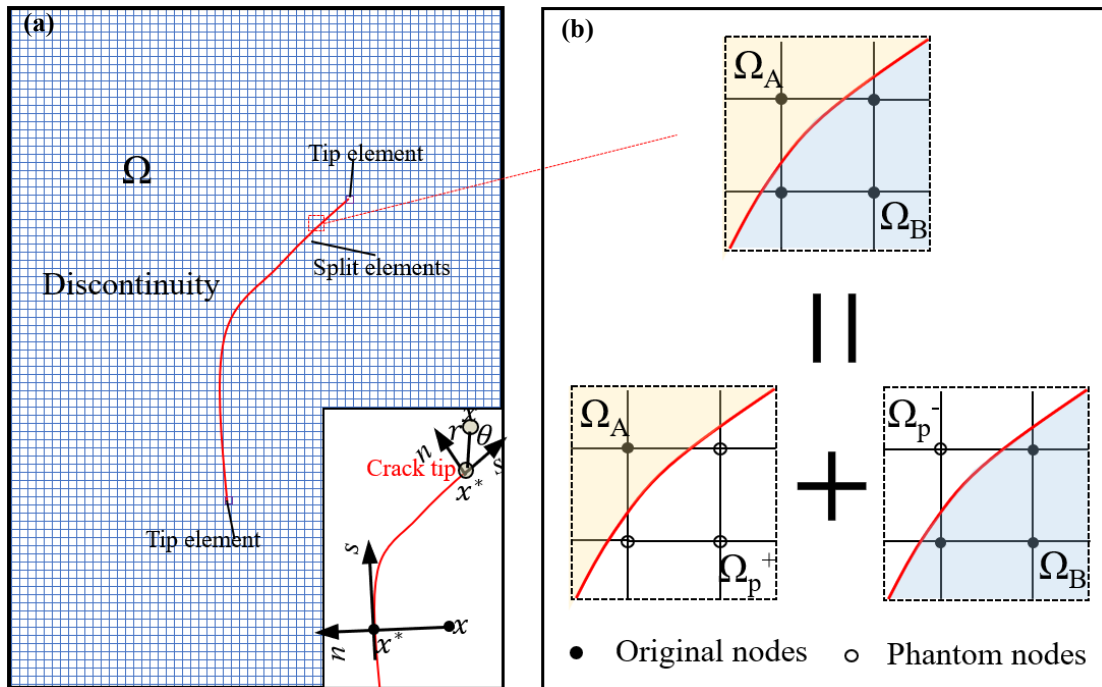


Fig. 2. Principles of the extended element method. (a) Sketch of a discontinuous element in the XFEM, (b) illustration of phantom node method.

127

128 Tensile strength of soil

129 Tensile cracks are generated by soil stretching (Fig. 3a), and Fig.3b shows a typical stress-displace curve
 130 of the tension process. Previous studies on tensile test for soil (Hadas and Lennard, 1988) show that a tensile
 131 crack forms when the tensile stress (σ_t) reaches the tensile strength (f_t). Before σ_t reaches f_t , the σ_t constantly
 132 increases with tensile displacement (Δl) (AB segment in Fig. 3b). In this stage, the tensile displacement

133 consists of elastic–plastic deformation of soil ($\Delta l_1 + \Delta l_3$ in Fig. 3a). When σ_t reaches f_t (point B in Fig. 3b),
 134 the soil is damaged and a crack forms. The start of damage leads to stress accumulation at the damaged part.
 135 And then, the accumulated stress is continuously released along the crack, causing crack propagation and
 136 opening. In this stage, σ_t decreases with the increase in Δl (BC segment in Fig. 3b), and the tensile
 137 deformation mainly consists of a crack opening, until the crack opening reaches the maximum value (Δl_2 in
 138 Fig. 3a). Finally, the soil body is completely separated (point C in Fig. 3b).

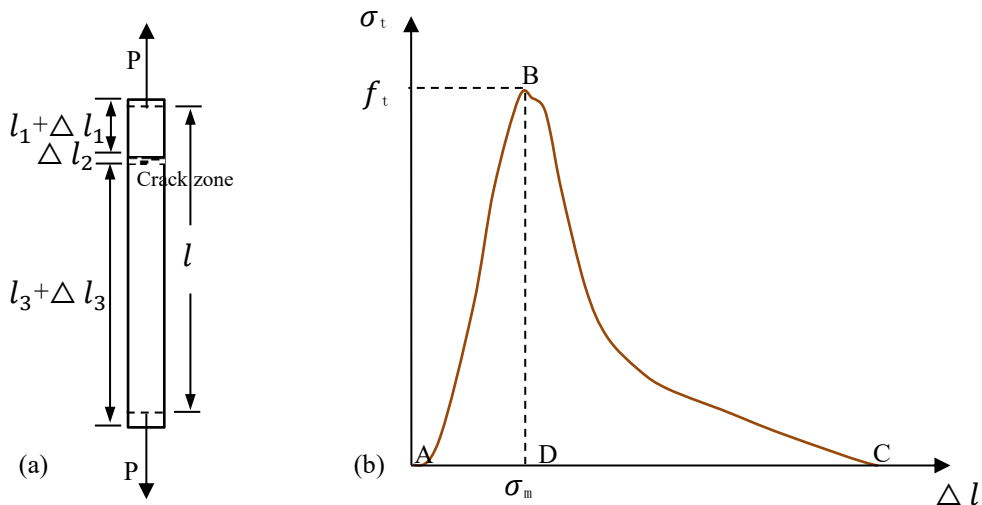


Fig. 3. Mechanical characteristics of the tensile crack of soil. (a) A sketch of tensile failure of materials, (b) an example of tensile stress–displacement curve of soil (modified from Tamrakar et al., 2005).

139

140 ABAQUS has several traction separation laws for material damage, and the maximum principal stress
 141 failure criterion (MAXPS) can be applied to the crack evolution of soil according to the above analysis. In the
 142 MAXPS criterion, no crack is generated until the maximum principal stress reaches a certain value; therefore,
 143 the value can be set as σ_t for the soil. The criterion of MAXPS can be expressed as follows:

144

$$f = \left\{ \frac{\langle \sigma_{max} \rangle}{\sigma_{max}^o} \right\}, \quad \langle \sigma_{max} \rangle = \begin{cases} 0, & \sigma_{max} < 0 \\ \sigma_{max}, & \sigma_{max} \geq 0 \end{cases} \quad (8)$$

145

where σ_{max}^o is the maximum allowed principle stress, determined from the tensile strength of soil. Damage is

146

initiated after the maximum principle stress reaches σ_{max}^o .

147

The crack expands in the direction perpendicular to the maximum principal stress after the initial damage,

148 and the evolution of an existing crack depends on the softening stage of the soil (BC segment in Fig. 3b).
 149 ABAQUS has two types of ways to define the softening stage: defining the maximum crack opening or fracture
 150 energy. When ignoring the plastic deformation during the cracking stage, the maximum crack opening can be
 151 considered as the length of DC segment, whereas the fracture energy can be considered as the area of DBC
 152 siege per length of material. The shape of softening phase curve (BC segment) can be specified by determining
 153 the form of index or discrete point data.

154 The composition of a soil slope usually includes clay, silt, sand, and gravel, considered as soil aggregates.
 155 To determine tensile parameters of soil aggregates, the authors studied some literature about tensile strength
 156 (Causarano et al., 1993; Hadas and Lennard, 1988; Munkholm et al., 2002; Tamrakar et al., 2005; Zhang et al.,
 157 2006) and found that their tensile strength usually ranges from several kilopascal to tens of kilopascal for soil
 158 aggregates (Table 1). Many factors such as density, water content, composition, and porosity affect the tensile
 159 properties of soils. In this paper, the authors used the stress–strain curve reported in Tamrakar’s research
 160 (Tamrakar et al., 2005) as a typical stress–strain curve (Fig. 3b) and applied it to all the simulation where damage
 161 evolution was attenuated in a quadratic form.

Table 1. A brief summary for tensile strength of soil aggregates

Material	Composition	Density (kg/m ³)	Water content (%)	particle diameter (mm)	Tensile strength (kPa)	Maximum crack opening (mm)	references
Soil aggregates	Clay-sand mixtures	1440	10	0.001-1	9	0.2	Tamrakar et al., 2005
	Sandy loam	1410-1570	30	2-16	2.0-3.2(compacted) 10-15(non-compacted)		Munkholm et al., 2002
	Sandy loam	\	5-20	\	10-25		Causarano et al., 1993
	Compacted gravel soil	1900-2200	16.3-19.3	\	30-80		Zhang et al., 2006
	Fine sand	2100-2200	3-35	0.01-1	0.26-1.2	0.02	Cai et al., 2017

162 Model validation

163 To evaluate whether XFEM can well analyze the behavior of tensile crack in soil, a numerical tensile test
164 was performed to calibrate it. The tensile test is referred from Tamrakar's study (Tamrakar et al., 2005). In the
165 test, a compacted clay-sand mixture specimen was stretched using a steel tensile mold at a steady velocity (Fig.
166 4a). The physical parameters of material were obtained from the research, whereas the damage parameters of
167 soil were obtained from the stress-displacement curve ($\sigma_{max}^o = 10$ kPa, the maximum crack = 0.2 mm). The
168 results show the progress in crack propagation generated by stretching, and the final figure of crack in the
169 simulation is consistent with the laboratory test (Fig. 4b-e), indicating that XFEM can well simulate the tensile
170 cracks in soil.

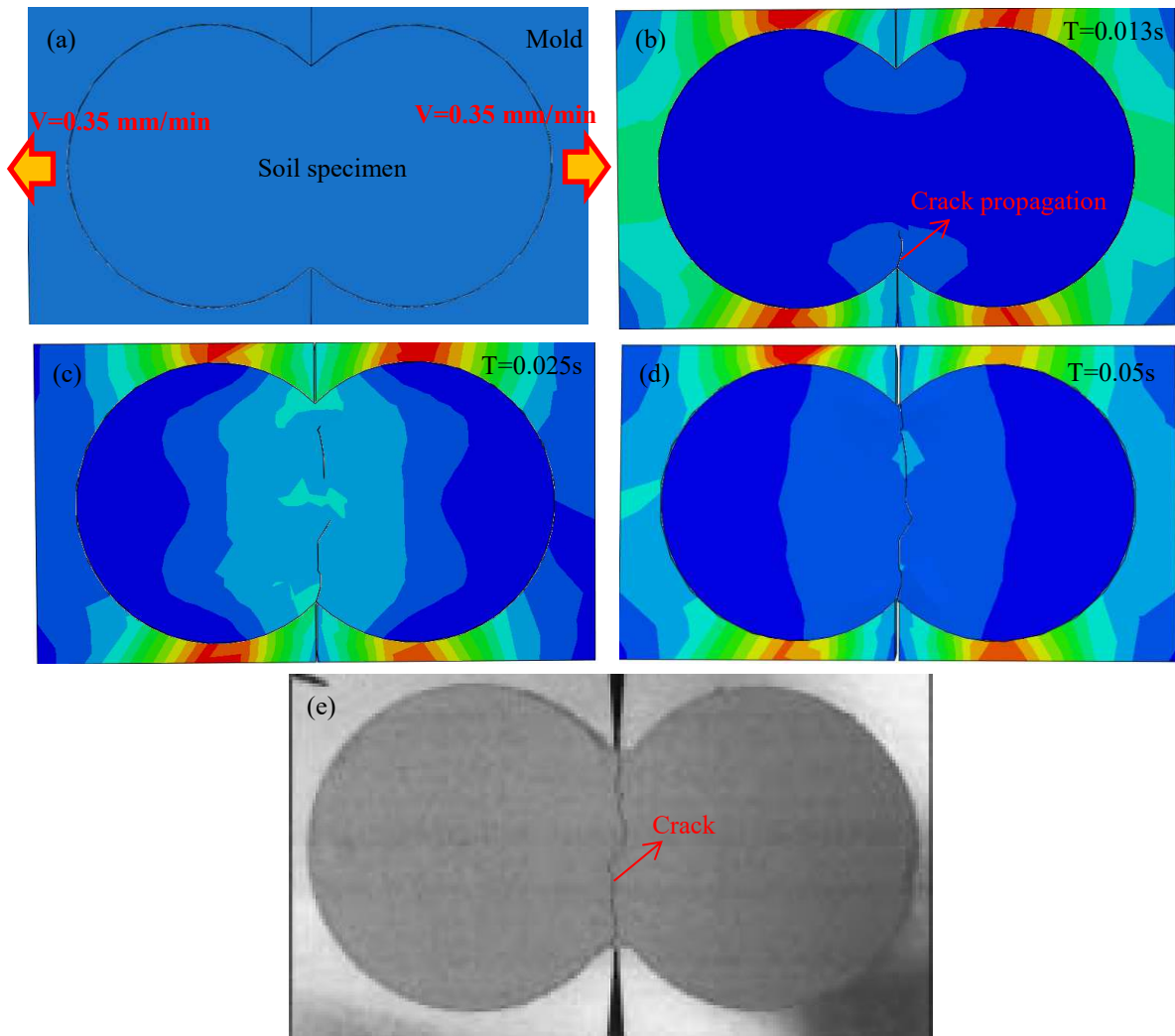


Fig. 4. Comparison result of real and simulation tensile tests. (a)–(d) Propagation of crack during the stretching based on the stress result, (e) tensile test in Tamrakar’s study (Tamrakar et al., 2005).

171

172 **Results and discussion**

173 Slope stability analysis

174 In this section, a two-dimensional (2D) slope model was used to evaluate whether XFEM can evaluate
 175 the slope stability with cracks. The model is a classic slope model with a toe angle of 45°, which has been
 176 widely used for the validation of slope stability (Bhandari et al., 2016; Wu et al., 2017). Its specific dimensions
 177 and boundary conditions are shown in Fig. 5a. Mechanical parameters of the soil were taken as γ (density) =
 178 2000 kg/m³, ϕ (internal angle of friction) = 34°, c (cohesion) = 10 kPa, ν (Poisson’s ratio) = 0.27, E (elasticity

179 modulus) = 40 MPa from Bao's literature of soil aggregates (Bao et al., 2019a); the tensile stress–strain curve
180 was adopted from Tamrakar's research and corresponding damage parameters of the soil were taken a relative
181 small value as $\sigma_{max}^o = 1$ kPa and the maximum crack opening = 0.02 mm. The stability of slope without XFEM
182 element and the slope using XFEM with an internal crack were calculated.

183 In the simulation, the failure of slope relied on the strength reduction technique (Matsui and San, 1992)
184 and the strength reduction factor (SRF), which have been widely applied to determine the potential slip surface
185 of a slope (Niant et al., 2012; Jiang et al., 2015; Bao et al., 2020). The phenomenon that plastic zone extends
186 from the toe to the upper of the slope was treated as the signal of failure (Shen and Karakus, 2014). Failure
187 criterion of the Mohr–Coulomb strength criterion was adopted for the material.

188 Figs. 5b–e show the results of stability analysis. After the strength reduction, the plastic strain zone expands
189 from the slope toe to upper. When plastic deformation reaches the position of internal crack, stress is transmitted
190 along the crack to the crack tip and causes stress accumulation. Stress at the tip of crack constantly increases
191 until it reaches the value of σ_{max}^o (1 kPa), causing crack propagation to the upper of slope. The FOS of slope
192 without crack is 1.298, whereas the FOS of slope with an internal crack is 1.281. From this simple case, it can
193 be considered that the cracks in the slope might affect the shape of potential slip surface and even the value of
194 FOS. In the following sections, we discuss several factors, including the position, strength, and depth of cracks
195 that might affect the stability of slope based on the above model.

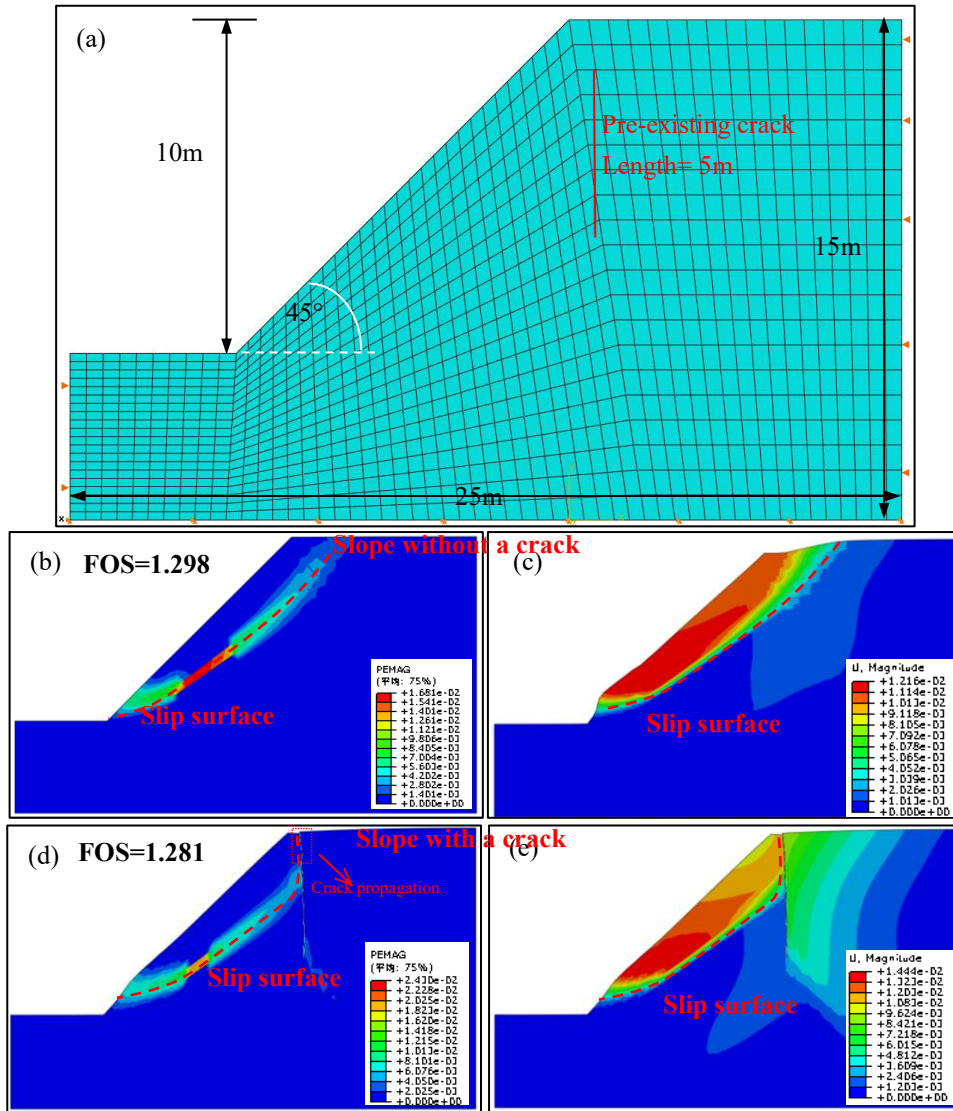


Fig. 5. Results of stability analysis. (a) Dimensions of the slope model, (b) and (d) magnitude of the plastic strain, (c) and (e) magnitude of the total displacement.

196

197 Sensitivity analysis

198 Fig. 6 shows the strength reduction of a slope without a pre-existing crack element when σ_{max}^0 is equal

199 to 5 kPa. The simulation result is consistent with the field investigation of most soil landslides. After strength

200 reduction, the slope is deformed towards the free surface with slope toe swelling (Fig.6a). Then a part of the

201 soil at the upper of slope gradually changes from compressive stress state to tensile stress state (Fig. 6d). When

202 the maximum tensile principal stress in the tension zone reaches the damage condition, damage starts (Figs. 6e

203 and f). The crack is formed at the slope crown, and the soils present on both sides of the crack have an obvious

204 vertical displacement difference when the slip surface is completely penetrated (Figs. 6g and h). This shows a
 205 typical failure mode of soil slopes in nature and proves that the crown crack is a signal of metastability.

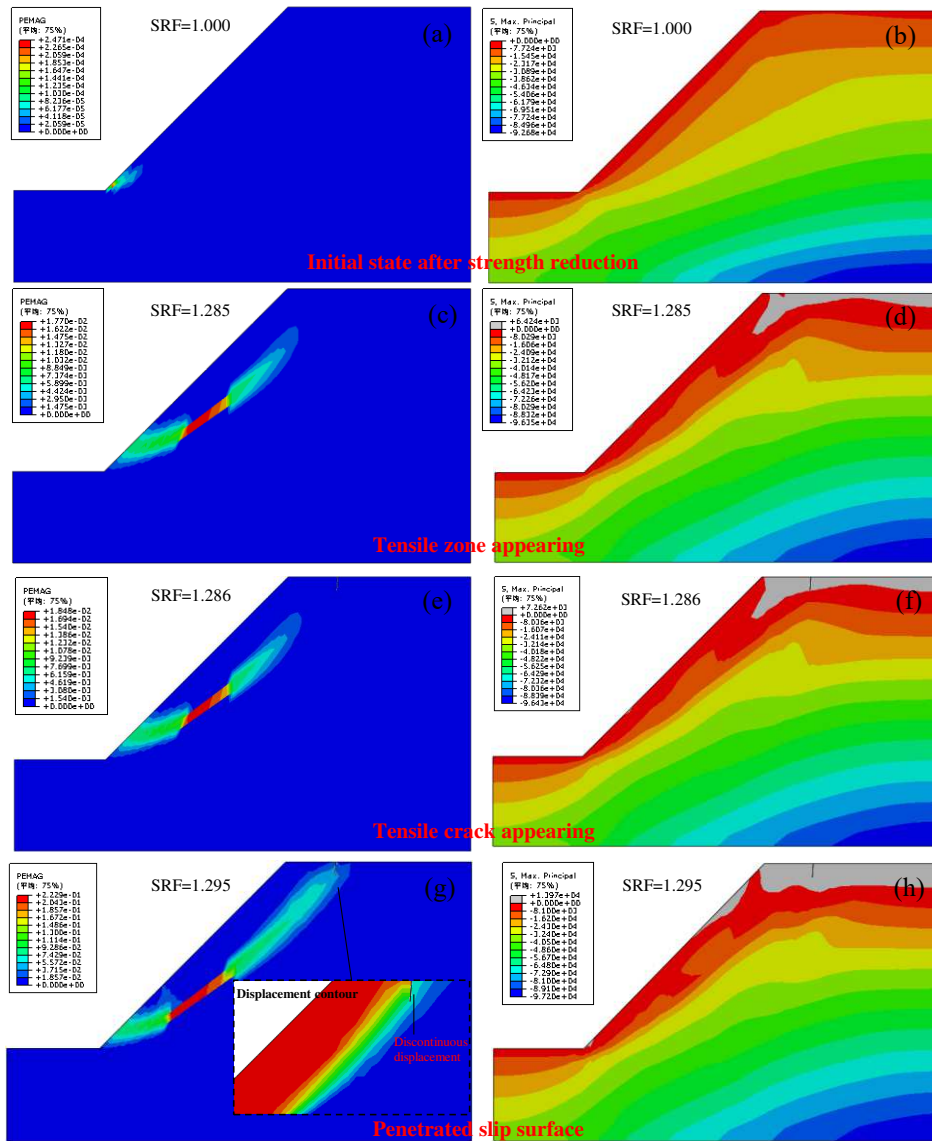


Fig. 6. Propagation of a tensile crack in a soil slope failure. (a), (c), (e), and (g) incorporate the contour map of plastic strain magnitude; (b), (d), (f), and (h) incorporate the contour map of maximum principal stress.

206

207 It's worth noting that the tensile crack appears and completely opens at the slope crown before the slip
 208 surface is penetrated (Fig. 6e and f). This means the length of shearing path of the slip surface is shorter than
 209 the entire length of slip surface, because the crack occupies a certain length of the slip surface. If a model does
 210 not consider tension effect or tensile cracks (e.g.: the conventional LEM assumes that the entire slip surface is
 211 generated by shear effect), the FOS calculated will be slightly larger than the real value. In the FEM simulation

212 of our case, the FOS of the slope is 1.298 when the plastic zone is completely penetrated without the XFEM
213 element, while the FOS is 1.295 when the plastic zone extends to the bottom of the tension crack with the
214 XFEM element.

215 In addition, the authors found the damage parameters of soil affect crack generation (Fig. 7). When the
216 value of σ_{max}^o is less than 4 kPa, the crack forms inside the potential failure mass (Figs. 7a and c), and the
217 displacement of soil on both sides of crack is continuous at the time of slope failure (Figs. 7b and d). When the
218 value of σ_{max}^o is more than 7.5 kPa, no crack is generated at the time of slope failure (Figs. 7g and h). Both
219 the situations are not consistent with field investigation and common sense, and seldom occur in reality (Tang
220 et al., 2019); thus, they are considered unreasonable. Only when the value of σ_{max}^o ranges from 4 kPa to 7.5
221 kPa, the simulation results such as Fig. 7e and Fig. 7f are consistent with the landslide field study. This
222 phenomenon can be attributed to soil strength. Bonds and friction exist between soil particles. They are
223 expressed as internal friction and cohesion in shearing, whereas they are expressed as tensile strength in tension.
224 Therefore, the tensile strength of soil is not completely independent of other strength parameters such as shear
225 strength. In the simulation, the value of cohesion is taken as 10 kPa while the internal friction is taken as 34°,
226 indicating that σ_{max}^o is a moderate value which is not too small or large. In other words, the tensile strength of
227 field soil in the scale of 4 kPa to 7.5 kPa is also moderate and appropriate. Although the relationship between
228 shear and tensile strength of soil requires more study, this speculation is supported by the results of numerical
229 simulation. This provides a new calibration idea to roughly estimate the tensile strength of soil, especially for
230 the field test which is difficult to conduct in a laboratory.

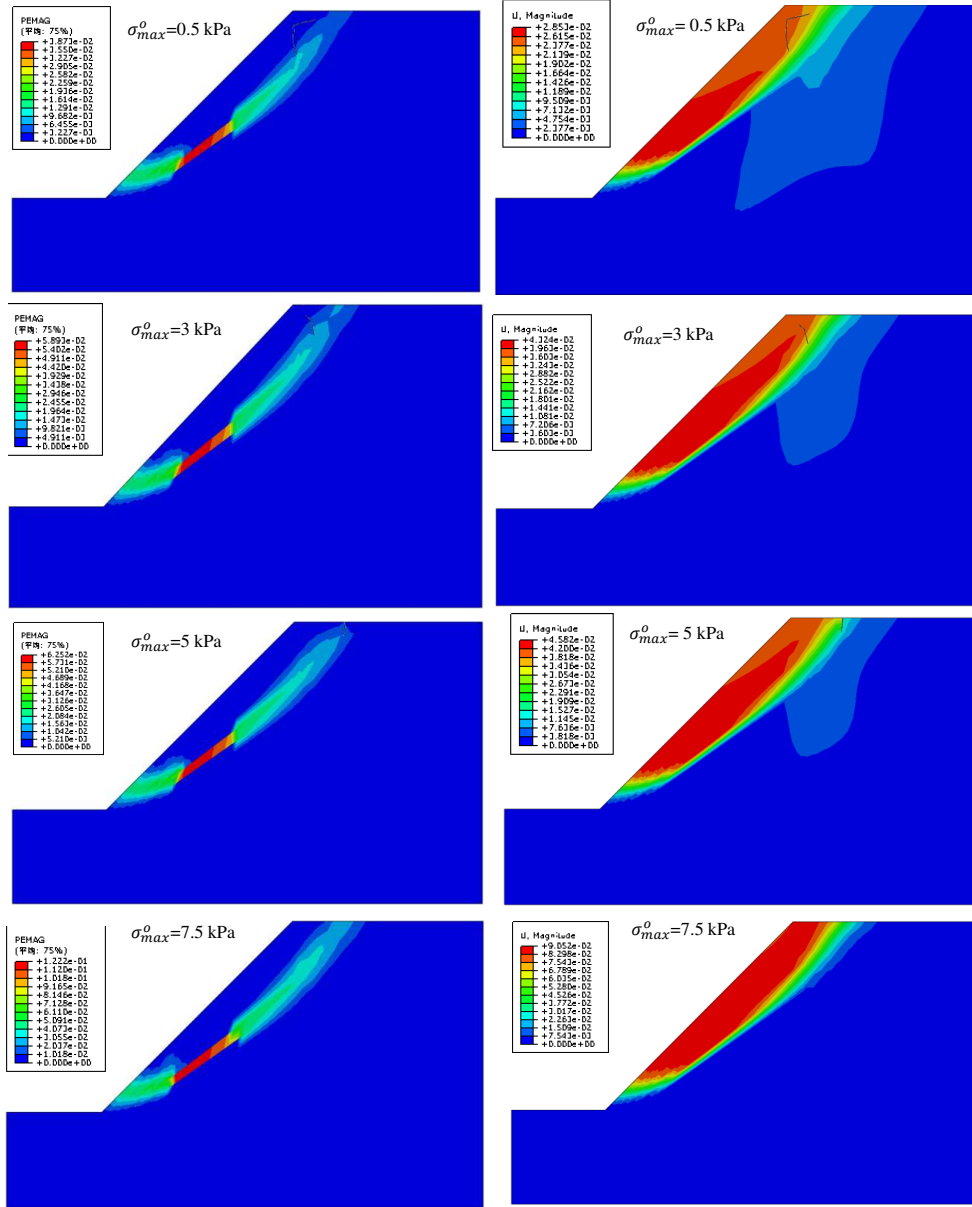


Fig. 7. Morphology of tensile crack at the time of a slope failure under different soil damage strengths. (a), (c), (e), and (g) the magnitude of plastic strain; (b), (d), (f), and (h) the magnitude of total displacement.

231

232

Besides the crown cracks, other types of tensile cracks generated by cycles of wetting and drying (Konrad

233

and Ayad, 1997), weathering (Hales and Roering, 2007), and desiccation (Peron et al., 2009) usually appear in

234

a slope. To explore whether tensile cracks affect stability of slope, six groups of numerical tests were set for

235

various situations, including the crack is located at the position of trailing edge, inside the potential failure zone,

236

and out of the potential failure zone (Fig.8). Considering that the strength of damage parameters might affect

237

the outcome, five groups of strength data that represent the very low, low, medium, high, and very high tensile

238 strength were used in the computation. σ_{max}^o was taken as 0.5, 2, 5, 20, and 50 kPa, and the corresponding
239 maximum crack opening was taken as 0.01, 0.04, 0.1, 0.4, and 1 mm, respectively, according to Fig.3b. Fig.9a-
240 f show the contour map of stress magnitude corresponding to Fig8a-f.

241 Fig. 8a shows the situation of a slope with a crack at the slope crown. The results show that the crack at
242 the slope crown hardly affects the stability of slope regardless of the strength of crack. This is probably because
243 the length of soil that can be sheared is very short at the slope crown, or the pre-existing penetrating crack
244 releases the accumulated stress and strain to the ground surface. Fig. 8b shows the situation of a slope with a
245 crack outside the potential failure zone. The results show that it is difficult for the tensile crack to affect the
246 stability of slope regardless of the length of crack and tensile strength of soil. Fig. 8c shows the situation of a
247 slope with a crack inside the potential failure zone. The results show that when the crack is very short and leaves
248 some distance to the potential plastic zone, it does not affect slope failure. When the crack is short but located
249 at the position of the potential plastic zone (Fig. 8d), it still generally does not affect the slope stability regardless
250 of the tensile strength of soil. This is because shearing is the mainly effect at this part of the slip surface, and
251 the phenomenon indicates this part of slope is at the compressive state. Fig. 8e shows a tensile crack with
252 relatively small damage parameters ($\sigma_{max}^o = 2$ kPa) that is at the upper part of potential slip surface. Compared
253 to Fig. 8d, the crack can be stretched to propagate to the ground surface after strength reduction. This is probably
254 because one tip of the crack is located at the tension zone (referring to Fig. 6h), changing the shape of original
255 slip surface and FOS in a smaller scale. One tip of the crack transmits stress, whereas the other tip accumulates
256 stress during strength reduction, and it determines the direction of propagation. When the crack propagates to
257 the ground surface, the accumulated stress is completely released (Fig. 9e). When the damage parameter
258 ($\sigma_{max}^o = 50$ kPa) is larger than the maximum tensile principal stress (13 kPa), the crack is not stretched, and the
259 potential slip surface does not change. Fig. 8f shows when a crack is much longer than the depth of original slip

260 surface, the presence of a crack causes stress redistribution after strength reduction, thus completely changing
 261 the original stress state and original potential slip surface (Fig. 9f).

262 Above all, the existence of cracks will cause discontinuities in stress (Fig.9). A crack completely buried
 263 underground will transmit stress on one tip, and accumulates stress on the other tip. If one tip of a crack
 264 propagates to the ground surface, all the accumulated stress will be released. Whether the tensile crack is pulled
 265 apart or not depends on the maximum tensile stress. According to the simulation, except the tension zone located
 266 on the upper of slope, the slope is generally at a compressive state, and it is difficult for a short-medium tensile
 267 crack in the compressive zone to change the original stability. Only a long tensile crack passed through the
 268 plastic zone, indicating that a large scale of stress redistribution will change the original stability.

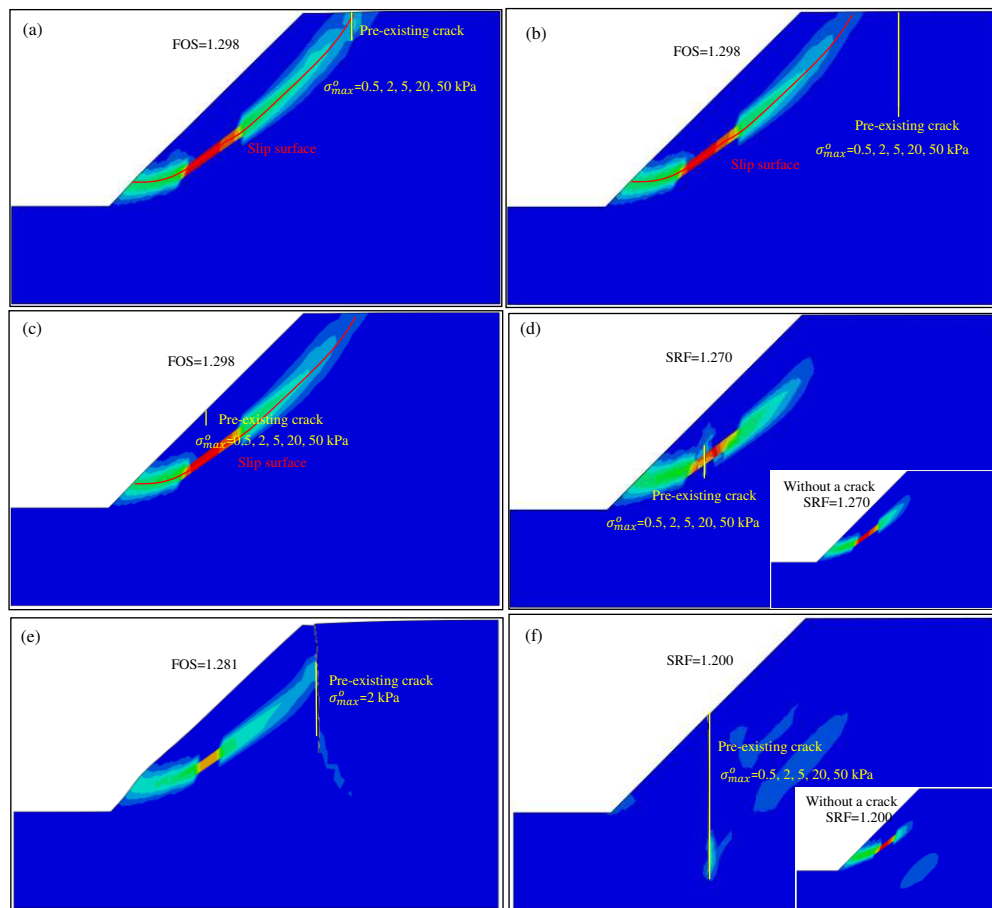


Fig. 8. Sensitivity analysis for crack propagation in different conditions based on the contour map of plastic strain magnitude.

269

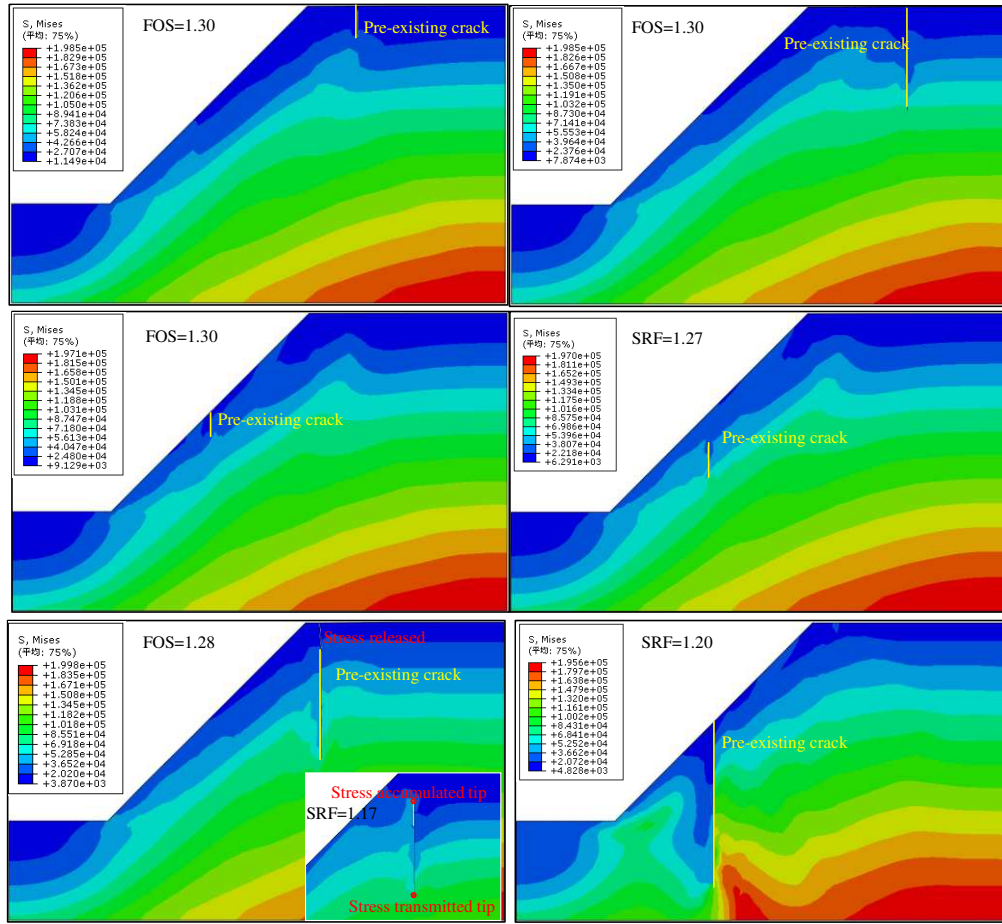


Fig. 9. Sensitivity analysis for crack propagation in different conditions based on the contour map of stress magnitude.

270

271

To determine the stress variation in slope from the initial deformation to failure, six nodes at different parts

272

of the slope were set to monitor the corresponding information (Fig. 10a). The maximum principal stress,

273

normal stress in the horizontal direction (s_{11}), normal stress in the vertical direction (s_{22}), and shear stress (s_{12})

274

were recorded. Fig. 10b shows when SRF is less than 1.25, the maximum principal stress is less than zero, and

275

the variation is very small with the increase in SRF value. In this scale of SRF, the slope is at a compressive

276

state, and no tensile crack is generated. When SRF is larger than 1.25, the maximum principal stress of the upper

277

of slope increases to a value of ~ 10 kPa, generating tensile cracks at the slope crown. Fig. 10c shows the

278

variation in S_{11} during the entire process. By comparing with Fig. 10b, it was observed that the direction of the

279

maximum principal stress is generally in the horizontal direction, leading to vertical cracks. Fig. 10d shows that

280 the slope of S22 is always less than zero owing to the presence of gravity and positively correlates with buried
 281 depth. Fig. 10e shows that the shear stress continuously increases around the zone of slip surface because the
 282 slip surface is mainly formed by the shear damage of soil. The stress state in slope illustrates the formation of
 283 crown cracks, and why most cracks in Fig. 8 cannot affect the slope stability.

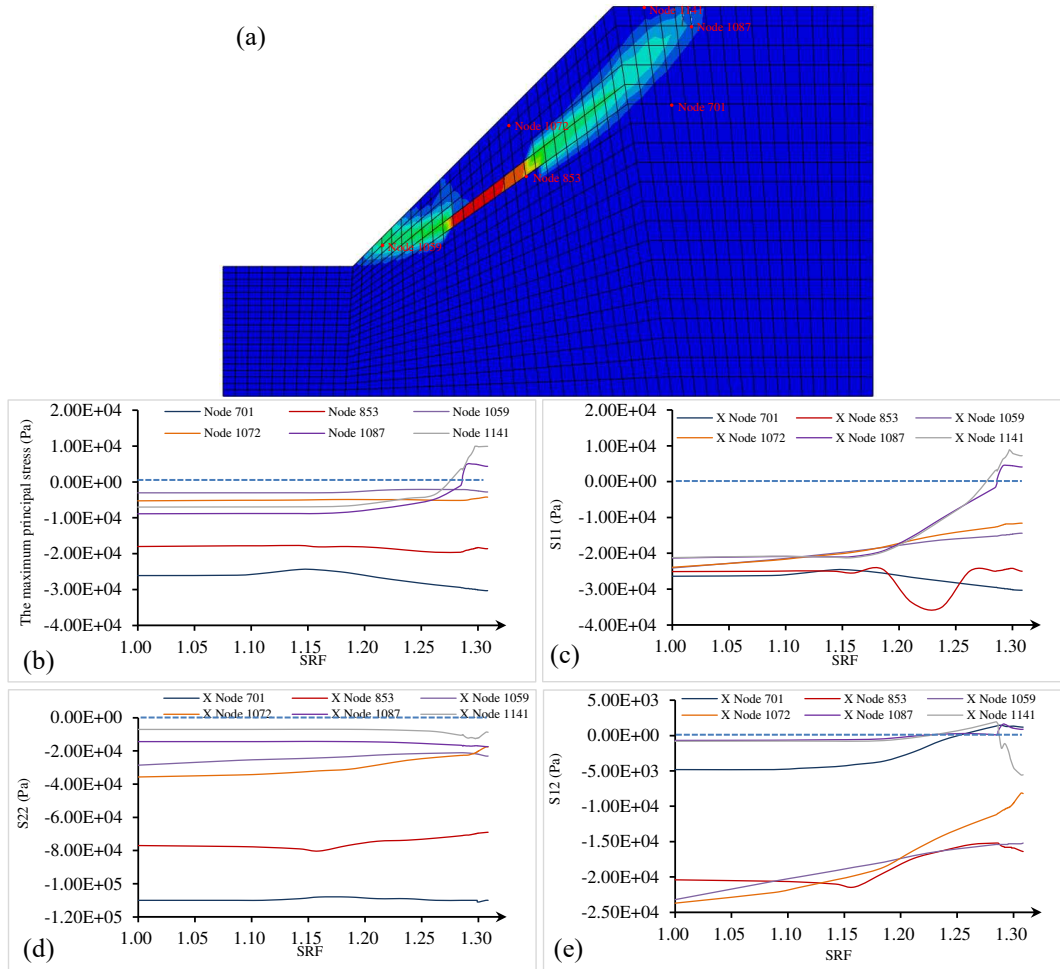


Fig. 10. Stress variation at different positions of slope. (a) Monitoring location of the model, (b) maximum principal stress of the monitoring nodes, (c) S11 of the monitoring nodes, (d) S22 of the monitoring nodes, and (e) S12 of the monitoring nodes.

284

285 Conclusions

286 This study aimed to illustrate the formation of crown cracks in a cohesive soil slope, and evaluate the effect
 287 of a tensile crack on slope stability using XFEM. The work is based on a numerical slope model with a toe angle
 288 of 45° and cohesion of 10 kPa. Tensile cracks with different damage parameters or lengths are set at different

289 positions in a slope model to achieve the goal. Some conclusions are drawn from the simulation.

290 1). The MAXPS based on XFEM well simulates the tensile behavior of soil. The XFEM model can
291 automatically search the position of cracks according to the stress field, avoiding pre-existing cracks in LEM,
292 and in the XFEM model the crack can develop with the computation. The FOS of the slope considering tensile
293 cracks is slightly smaller than the FOS of the slope without considering tensile cracks.

294 2). When the potential slip surface starts to penetrate, a tensile crack appears at the slope crown while
295 swelling occurs at the foot of the slope. The phenomenon can be considered as a signal of metastability of soil
296 slope before complete failure.

297 3). The initial stress state of a slope is at a compressive state. With slope deformation, the tension zone
298 appears on the upper of slope when the potential slip surface starts to penetrate. The stress field illustrates the
299 question in Tang's literature (Tang et al., 2019) why the depth of a crack cannot develop downward without
300 limitation.

301 4). Most of the tensile cracks in slopes hardly affect the slope stability. This is because of the compressive
302 stress state existing in most part of the slope. However, there are still two kinds of tensile cracks can affect
303 original slip surface or slope stability, cracks located in the tension zone or cracks passing through the potential
304 plastic zone with a long length.

305 5). During crack propagation, one tip of the crack transmits stress, and the other tip accumulates stress and
306 strain. The direction of propagation is from the transmitted tip to the accumulated tip, and accumulated stress
307 is released when the crack propagates to the ground surface.

308 These conclusions can guide the practical engineering in some aspects. For example, it is difficult to
309 determine the tensile strength of soil slopes. However, researchers can obtain the tensile parameters of soil by
310 calibrated the position of crown cracks based on the numerical simulation of slope stability. And researchers

311 can evaluate the extent of slope deformation by comparing the depth of crown cracks or the depth of drop heads
312 between the actual slope and numerical model.

313 It is noted that the slope model in the case has a toe angle of 45° and cohesion of 10kPa, representing one
314 type of soil slide (Fig.1). If a slope is mainly composed of sand, with lower cohesion or tensile strength, or has
315 steeper angle, it's more prone to collapse (Tang et al., 2019). And above conclusions are based on the condition
316 that seepage in cracks is not considered. Actually, water easily penetrates into the crack (Chen et al., 2019),
317 causing crack propagation (Zhou et al., 2009), and even lead to the landslide (Zhang et al., 2012). In addition,
318 water seepage along the crack will cause an increase in pore water pressure in the lower soil and produce
319 lubrication, thus macroscopically demonstrating that the shear strength in lower soil is reduced. How to consider
320 these complex interactions and behavior in a numerical model is still a difficult and challenging work.

321 **Declarations**

322 **Conflict of interest** The authors have no financial or proprietary interests in any material discussed in
323 this article.

324 **Acknowledgements**

325 This study was funded by the Strategic Priority Research Program of the Chinese Academy of Sciences
326 (Grant No. XDA20030301), National Natural Science Foundation (41790432), and the fellowship of China
327 Postdoctoral Science Foundation (No.2020M683369).

328 **References**

329 1. Areias, P.P., Rabczuk, T.T., Disa-da Costa, D.D., 2013. Element-wise fracture algorithm using the screened

- 330 poisson equation and local remeshing. *Eng. Fract. Mech.* 110, 113-137.
- 331 2. Areias, P.P., Reinoso, J.J., Camanho, P.P., Rabczuk, T.T., 2015. A constitutive-based element-by-element
332 crack propagation algorithm with local mesh refinement. *Comput. Mech.* 56 (2), 291-315.
- 333 3. Bao, Y., Han, X., Chen, J., Zhang, W., Zhan, J., Sun X., Chen, M., 2019. Numerical assessment of failure
334 potential of a large mine waste dump in Panzhihua City, China. *Engineering Geology* 253,171-183.
- 335 4. Bao, Y., Zhai, S., Chen, J., Xu, P., Sun, X., Zhan, J., Zhang, W., Zhou, X., 2020. The evolution of the
336 Samaoding paleo-landslide river blocking event at the upstream reaches of the Jinsha River, Tibetan Plateau.
337 *Geomorphology* 351. <https://doi.org/10.1016/j.geomorph.2019.106970>
- 338 5. Bhandari, T., Hamad, F., Moormann, C., Sharma, K. G., Westrich, B., 2016. Numerical modelling of
339 seismic slope failure using mpm. *Computers and Geotechnics*, 75, 126-134.
- 340 6. Bishop, A.W., 1973. The stability of tips and spoil heaps. *Journal of Experimental Biology* (6): 1851-
341 61.<https://doi.org/10.1144/GSL.QJEG.1973.006.03.15>
- 342 7. Causarano, H., 1993. Factors affecting the tensile strength of soil aggregates. *Soil and Tillage Research*,
343 28, 15-25.
- 344 8. Cai G, Che R, Kong X, Liu C, Zhao C (2017) Experimental investigation on tensile strength of unsaturated
345 fine sands. *Journal of Hydraulic Engineering* (48): 623-631 (In Chinese).
- 346 9. Chen, H., Qin, S., Xue, L., Yang, B., Zhang, K., 2018a. A physical model predicting instability of rock
347 slopes with locked segments along a potential slip surface. *Engineering Geology* 242, 34-43.
- 348 10. Chen, K., Wu, J., 2018b. Simulating the failure process of the Xinmo landslide using discontinuous
349 deformation analysis. *Engineering Geology* 239, 269-281.
- 350 11. Chen, Z., Song, D., Hu, C., Ke, Y., 2019. The September 16, 2017, Linjiabang landslide in Wanyuan
351 County, China: preliminary investigation and emergency mitigation. *Landslides*. DOI 10.1007/s10346-

- 352 019-01309-1
- 353 12. Conte, E., Pugliese, L., Troncone, A., 2019. Post-failure stage simulation of a landslide using the material
354 point method. *Engineering Geology* 253, 149-159.
- 355 13. Fan, X., Xu, Q., Gianvito, S., Zheng, G., Huang, R., Dai, L., Ju, Y., 2018., The “long” runout rock
356 avalanche in Pusa, China, on August 28, 2017: a preliminary report. *Landslides*. DOI 10.1007/s10346-
357 018-1084-z
- 358 14. Fan, X., Xu, Q., Liu, J., Subramanian, S., He, Chao., Zhu, X., Zhou, L., 2019. Successful early warning
359 and emergency response of a disastrous rockslide in Guizhou province, China. *Landslides*. DOI
360 10.1007/s10346-019-01269-6.
- 361 15. Griffiths, D. V., Lane, P. A. 1999. Slope stability analysis by finite elements. , 49(7), 653-654.
- 362 16. Gianvito, S., Xuanmei, F., Qiang, X., Chun, L., Chaojun, O., Domènech, Guillem., Fan, Y., Lanxi, D.,
363 2018. Some considerations on the use of numerical methods to simulate past landslides and possible new
364 failures: the case of the recent Xinmo landslide (Sichuan, China). *Landslides* 15, 1359–1375.
- 365 17. Guo, C., Zhang, Y., Li, X., Ren, S., Yang, Z., Wu, R., Jin, J., 2019. Reactivation of giant Jiangdingya
366 ancient landslide in Zhouqu County, Gansu Province, China. *Landslides*. DOI 10.1007/s10346-019-
367 01266-9
- 368 18. Hadas, A., Lennard, G., 1988. Dependence of tensile strength of soil aggregates on soil constituents,
369 density and load history. *European Journal of Soil Science* (39), 577-586.
- 370 19. Hales, T.C., Roering, J.J., 2007. Climatic controls on frost cracking and implications for the evolution of
371 bedrock landscapes. *Journal of Geophysical Research Earth Surface* 2007, 112(F2), 2003-2012.
372 <https://doi.org/10.1029/2006JF000616>
- 373 20. Hungr, O., Leroueil, S., Picarelli, L., 2014. The Varnes classification of landslide types, an update.

- 374 Landslides 11, 167-194.
- 375 21. Jiang, Q., Qi, Z., Wei, W. & Zhou, C.B. 2015. Stability assessment of a high rock slope by strength
376 reduction finite element method. *Bulletin of Engineering Geology and the Environment*, 74, 1153–1162.
- 377 22. Koerner, R.M., Soong, T.Y., 2000. Stability Assessment of Ten Large Landfill Failures. *Geo-Denver*, 1-38.
- 378 23. Konrad, J.M., Ayad, R., 1997. An idealized framework for the analysis of cohesive soils undergoing
379 desiccation. *Canadian Geotechnical Journal* 34(4), 477-488.
- 380 24. Lei, H., Liu, X., Song, Y., Xu, Y., 2021. Stability analysis of slope reinforced by double-row stabilizing
381 piles with different locations. *Natural Hazards* 106, 19-42.
- 382 25. Li, L., Wang, Y., Zhang, L., Choi, C., Ng, C.W.W., 2019. Evaluation of Critical Slip Surface in Limit
383 Equilibrium Analysis of Slope Stability by Smoothed Particle Hydrodynamics. *International Journal of*
384 *Geomechanics* 19, 5.
- 385 26. Liu, X., Wang, Y., Li, D., 2019. Investigation of slope failure mode evolution during large deformation in
386 spatially variable soils by random limit equilibrium and material point methods. *Computers and*
387 *Geotechnics*, 301-312.
- 388 27. Lo, C., Lin, M., Tang, C., Hu, C., 2011. A kinematic model of the Hsiaolin landslide calibrated to the
389 morphology of the landslide deposit. *Engineering Geology* 123, 22-39.
- 390 28. Ma, G.W., An, X.M., Zhang, H.H., Li, L.X., 2009. Modeling complex crack problems using the numerical
391 manifold method. *Int. J. Fract.* 156:21-35
- 392 29. Matsui, T., San, K.C., 1992. Finite element slope stability analysis by shear strength reduction technique.
393 *Soils and Foundations* 32, 59-70.
- 394 30. Michalowski, R.L., 2012. Cracks in slopes: limit analysis approach to stability assessment. *GeoCongress*
395 2012: State of the Art and Practice in Geotechnical Engineering. ASCE, pp. 442–450.

396 <http://dx.doi.org/10.1061/9780784412121.046>.

397 31. Michalowski, R.L., 2013. Stability assessment of slopes with cracks using limit analysis. *Can. Geotech. J.*
398 50, 1011–1021.

399 32. Moës, N., Dolbow, J., Belytschko, T., 1999. A finite element method for crack growth without remeshing.
400 *International Journal for Numerical Methods in Engineering* 46, 131-150.

401 33. Munkholm, L.J., Schjønning, P., Kay, B.D., 2002. Tensile strength of soil cores in relation to aggregate
402 strength, soil fragmentation and pore characteristics. *Soil & Tillage Research* (64), 125-135.

403 34. Niant, K., Huanger, Q., Wans, S. Cheng, Q. 2012. Three-dimension strength reduction finite element
404 analysis of slopes: geometric effects. *Canadian Geotechnical Journal*, 49, 574–588

405 35. Ouyang, C., An, H., Zhou, S., Wang, Z., Su, P., Wang, D., Cheng, D., She, J., 2019 Insights from the failure
406 and dynamic characteristics of two sequential landslides at Baige village along the Jinsha River, China.
407 *Landslides* DOI 10.1007/s10346-019-01177-9

408 36. Peron, H., Hueckel, T., Laloui, L., Hu, L.B., 2009. Fundamentals of desiccation cracking of finegrained
409 soils: experimental characterization and mechanisms identification. *Canadian Geotechnical Journal* 46(1),
410 1177-1201.

411 37. Qu, G., Hinchberger, S.D., Lo, K.Y., 2009. Case studies of three-dimensional effects on the behaviour of
412 test embankments. *Canadian Geotechnical Journal* 46, 1356-1370.

413 38. Rabczuk, T., Ren, H., 2017. A peridynamics formulation for quasi-static fracture and contact in rock.
414 *Engineering Geology* 225, 42-48.

415 39. Ray, R., Deb, K., Shaw, A., 2019. Pseudo-Spring smoothed particle hydrodynamics (SPH) based
416 computational model for slope failure. *Engineering Analysis with Boundary Elements* 101, 139-148.

- 417 40. Sanborn, S.E., Jean H, P., 2011. Frictional slip plane growth by localization detection and the extended
418 finite element method (XFEM). *International Journal for Numerical & Analytical Methods in*
419 *Geomechanics* 35, 11, 1278-1298.
- 420 41. Seed, R.B., Mitchell, J.K., Seed, H.B., 1990. Kettleman Hills Waste Landfill Slope Failure. II: Stability
421 Analyses. *Journal of Geotechnical and Geoenvironmental Engineering* 116, 669-690.
- 422 42. Shen, J., Karakus, M., 2014. Three-dimensional numerical analysis for rock slope stability using shear
423 strength reduction method. *Canadian Geotechnical Journal* 51, 164-172.
- 424 43. Shi, G.-H., 1991. Manifold method of material analysis. *Transaction of the 9th Army Conference on*
425 *Applied Mathematics and Computing*. Minneapolis, Minnesota, USA, pp, 57-76
- 426 44. Solari, L., Raspini, F., Del Soldato, M., Bianchini, S , Ciampalini, A., Ferrigno, F., et al. 2018. Satellite
427 radar data for back-analyzing a landslide event: the ponzano (central italy) case study. *Landslides*, 15(4),
428 773-782.
- 429 45. Steiakakis, E., Kavouridis, K., Monopolis, D., 2009. Large scale failure of the external waste dump at the
430 “South Field” lignite mine, Northern Greece. *Engineering Geology* 104, 269-279.
- 431 46. Tamarkar, S.B., Totosawa, Y., Itoh, K., 2005. Tensile Strength of Soil Measured Using Newly Developed
432 Tensile Strength Apparatus. *Research Reports of the National Institute of Industrial Safety*.
- 433 47. Tang, C., Hu, J., Lin, M., Angelier, J., Lu, C., Chan. Y., Chu, H., 2009. The Tsaoiling landslide triggered
434 by the Chi-Chi earthquake, Taiwan: insights from a discrete element simulation. *Eng Geol* 106, 1–19.
- 435 48. Tang, L., Zhao, Z., Luo, Z., Sun, Y., 2019. What is the role of tensile cracks in cohesive slopes?. *Journal*
436 *of Rock Mechanics and Geotechnical Engineering* 11, 314-324.

- 437 49. Wang, G.H., Wang, Y.X, Lu, W.B., Zhou, C.B, Chen, M., Peng, Y., 2015. XFEM based seismic potential
438 failure mode analysis of concrete gravity dam–water–foundation system through incremental dynamic
439 analysis. *Engineering Structures* 98, 81-94.
- 440 50. Wu, L.Z., Zhou, Y., Sun, P., Shi, J.S., Liu, G.G., Bai, L.Y., 2017. Laboratory characterization of rainfall-
441 induced loess slope failure. *Catena* 150, 1-8.
- 442 51. Xu, Q., Zheng, G., Li, W., He, C., Dong, X., Guo, X., Feng, W., 2018. Study on successive landslide
443 damming events of Jinsha River in Baige Village on October 11 and November 3. *Journal of Engineering
444 Geology*, 26, 1534-1551.
- 445 52. Yin, Y.P., Li, B., Wang, W.P., Zhan, L.T., Xue, Q., Gao, Y., Zhang, N., Chen, H.Q., Liu, T.K., Li, A.G.,
446 2016. Mechanism of the december 2015 catastrophic landslide at the Shenzhen landfill and controlling
447 geotechnical risks of urbanization. *Engineering* 2, 230–249.
- 448 53. Zhang, F., Yan, B., Feng, X., Lan, H., Kang, C., Lin, X., Zhu, X., Ma, W., 2019a. A rapid loess mudflow
449 triggered by the check dam failure in a bulldoze mountain area, Lanzhou, China. *Landslides* 10, 1981-
450 1992.
- 451 54. Zhang, G., Wang, R., Qian, J., Zhang, J., Qian, J., 2012. Effect study of cracks on behavior of soil slope
452 under rainfall conditions. *Soils and Foundations* 52, 4, 634-643.
- 453 55. Zhang, H., Zhu, J., Wang, J., Yuan, Y., Feng, Lin., 2006. Experimental study of tensile strength of
454 compacted gravel soil. *Chinese Journal of Rock Mechanics and Engineering* 25, 4186-4190.
- 455 56. Zhou, J., Wang, J.Q., Zeng, Y., Zhang, J., 2009. Simulation of slope stability analysis by particle flow code.
456 *Rock Soil Mech* 30(1), 86–90.
- 457 57. Zhou, X., Chen, J., 2019. Extended finite element simulation of step-path brittle failure in rock slopes with
458 non-persistent en-echelon joints. *Engineering Geology* 250, 65-88.

- 459 58. Zhou, Y. D., Cheuk, C. Y., Tham, L. G., 2009. Deformation and crack development of a nailed loose fill
460 slope subjected to water infiltration. *Landslide* 6, 299-308.
461
462

463 **Lists of figures**

464 **Fig. 1.** Crown cracks appear in some soil slopes. (a) A potential landslide with obvious deformation in Jilin
465 province in 2016, (b) a potential landslide in a waste dump in Sichuan province in 2016, (c) a potential landslide
466 with obvious deformation in Jilin province in 2015, and (d) a potential landslide in Liaoning province in 2019.
467 Red Arrows denote to the direction of slides.

468 **Fig. 2.** Principles of the extended element method. (a) Sketch of a discontinuous element in the XFEM, (b)
469 illustration of phantom node method.

470 **Fig. 3.** Mechanical characteristics of the tensile crack of soil. (a) A sketch of tensile failure of materials, (b) an
471 example of tensile stress–displacement curve of soil (modified from Tamrakar et al., 2005).

472 **Fig. 4.** Comparison result of real and simulation tensile tests. (a)–(d) Propagation of crack during the stretching
473 based on the stress result, (e) tensile test in Tamrakar’s study (Tamrakar et al., 2005).

474 **Fig. 5.** Results of stability analysis. (a) Dimensions of the slope model, (b) and (d) magnitude of the plastic
475 strain, (c) and (e) magnitude of the total displacement.

476 **Fig. 6.** Propagation of a tensile crack in a soil slope failure. (a), (c), (e), and (g) incorporate the contour map of
477 plastic strain magnitude; (b), (d), (f), and (h) incorporate the contour map of maximum principal stress.

478 **Fig. 7.** Morphology of tensile crack at the time of a slope failure under different soil damage strengths. (a), (c),
479 (e), and (g) the magnitude of plastic strain; (b), (d), (f), and (h) the magnitude of total displacement.

480 **Fig. 8.** Sensitivity analysis for crack propagation in different conditions based on the contour map of plastic
481 strain magnitude.

482 **Fig. 9.** Sensitivity analysis for crack propagation in different conditions based on the contour map of stress
483 magnitude.

484 **Fig. 10.** Stress variation at different positions of slope. (a) Monitoring location of the model, (b) maximum

485 principal stress of the monitoring nodes, (c) S11 of the monitoring nodes, (d) S22 of the monitoring nodes,

486 and (e) S12 of the monitoring nodes.

487 **Lists of tables**

488 **Table.1** A brief summary for tensile strength of soil aggregates

Figures



Figure 1

Crown cracks appear in some soil slopes. (a) A potential landslide with obvious deformation in Jilin province in 2016, (b) a potential landslide in a waste dump in Sichuan province in 2016, (c) a potential landslide with obvious deformation in Jilin province in 2015, and (d) a potential landslide in Liaoning province in 2019. Red Arrows denote to the direction of slides.

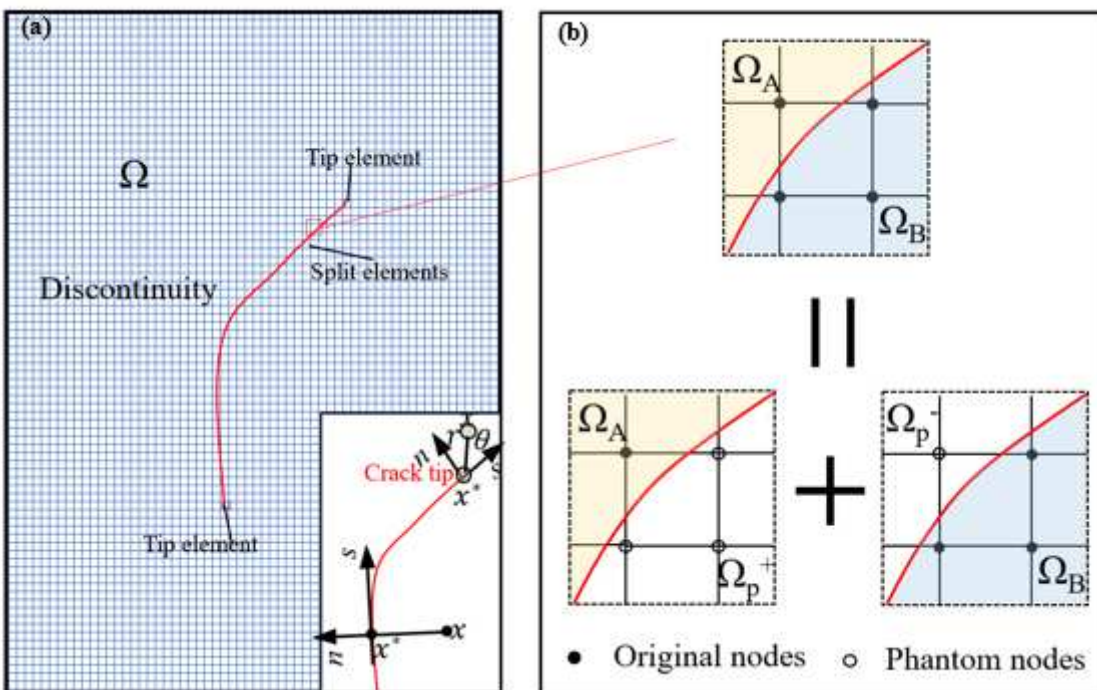


Figure 2

Principles of the extended element method. (a) Sketch of a discontinuous element in the XFEM, (b) illustration of phantom node method.

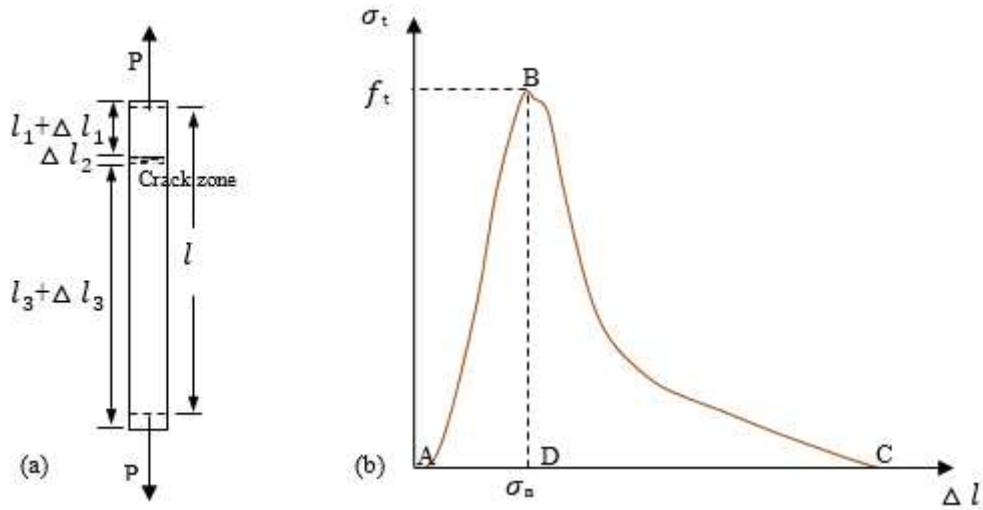


Figure 3

Mechanical characteristics of the tensile crack of soil. (a) A sketch of tensile failure of materials, (b) an example of tensile stress-displacement curve of soil (modified from Tamrakar et al., 2005).

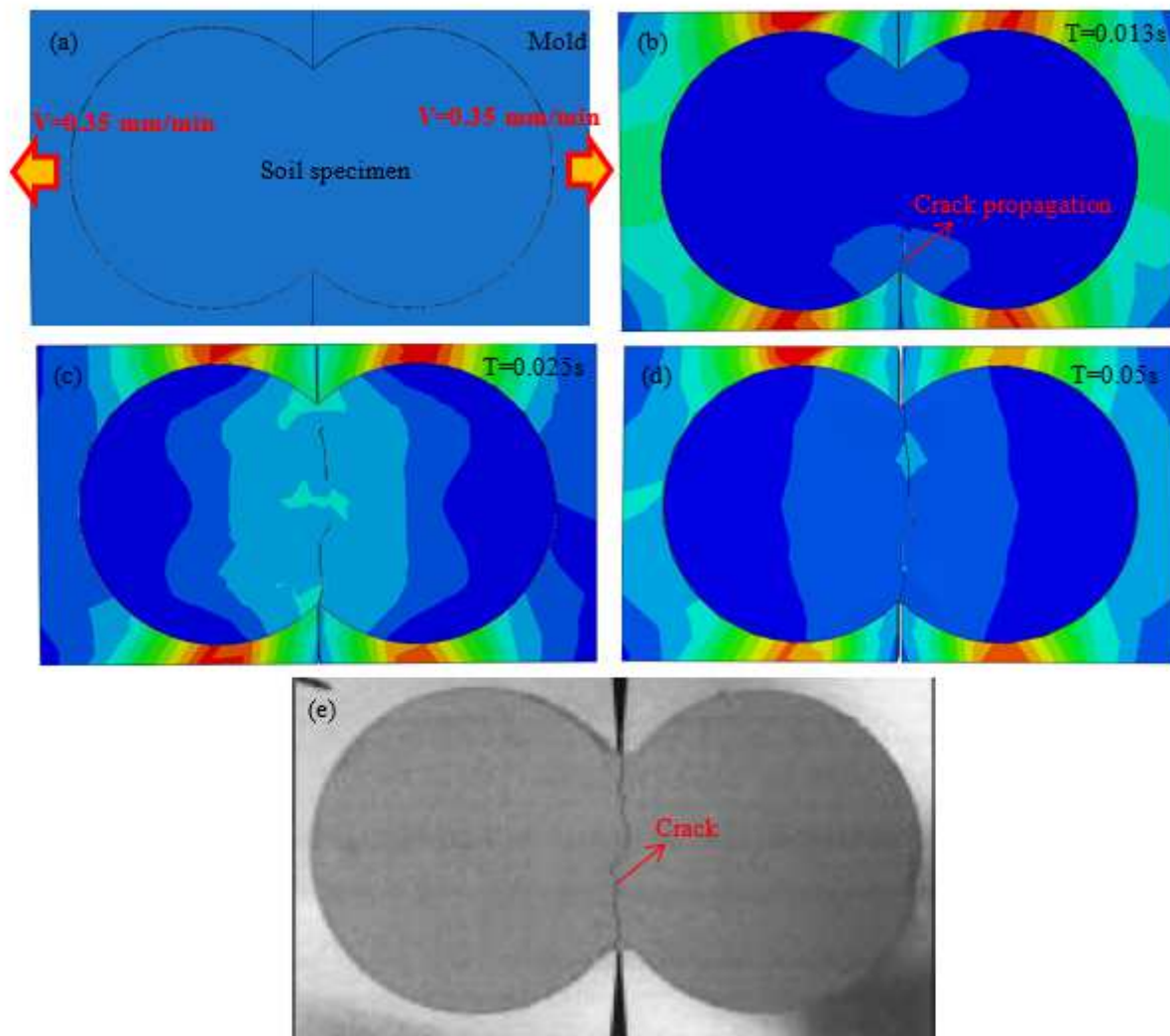


Figure 4

Comparison result of real and simulation tensile tests. (a)–(d) Propagation of crack during the stretching based on the stress result, (e) tensile test in Tamrakar’s study (Tamrakar et al., 2005).

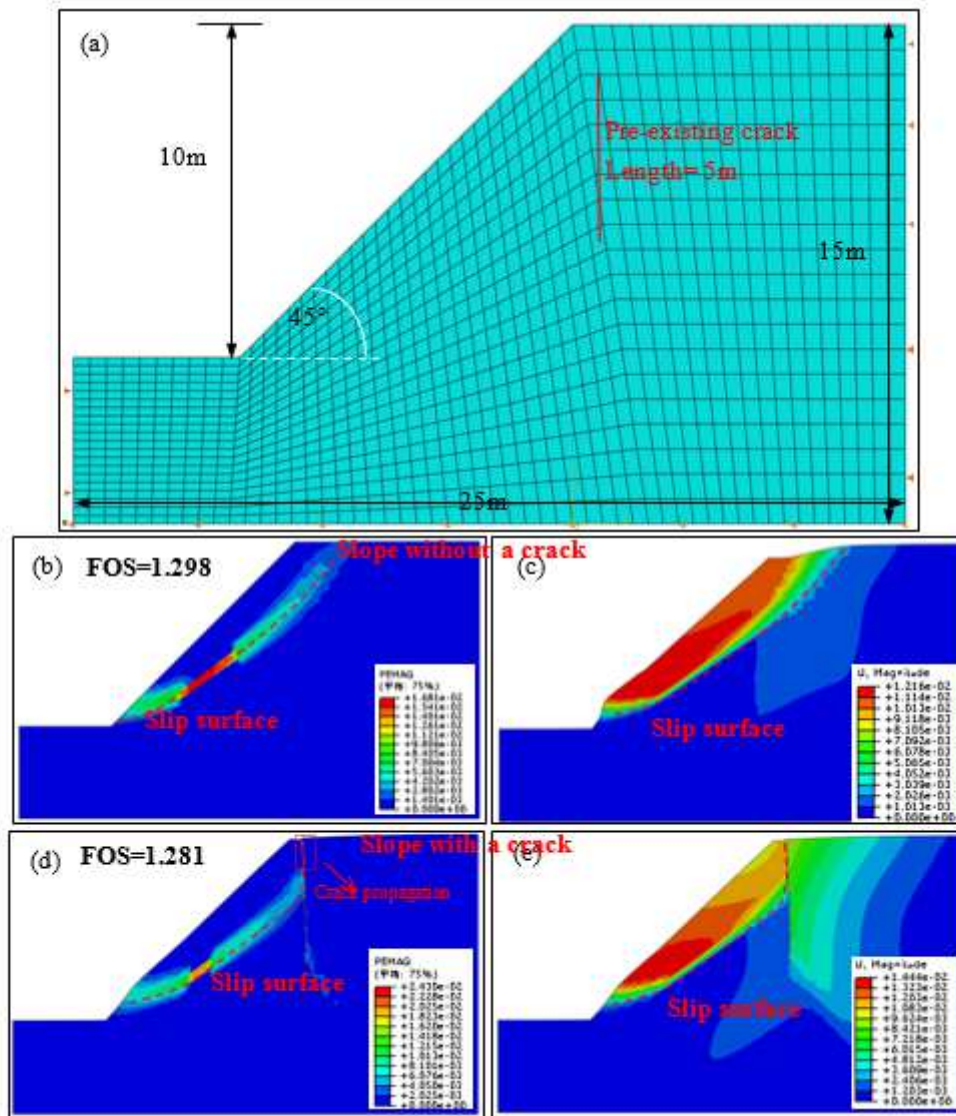


Figure 5

Results of stability analysis. (a) Dimensions of the slope model, (b) and (d) magnitude of the plastic strain, (c) and (e) magnitude of the total displacement.

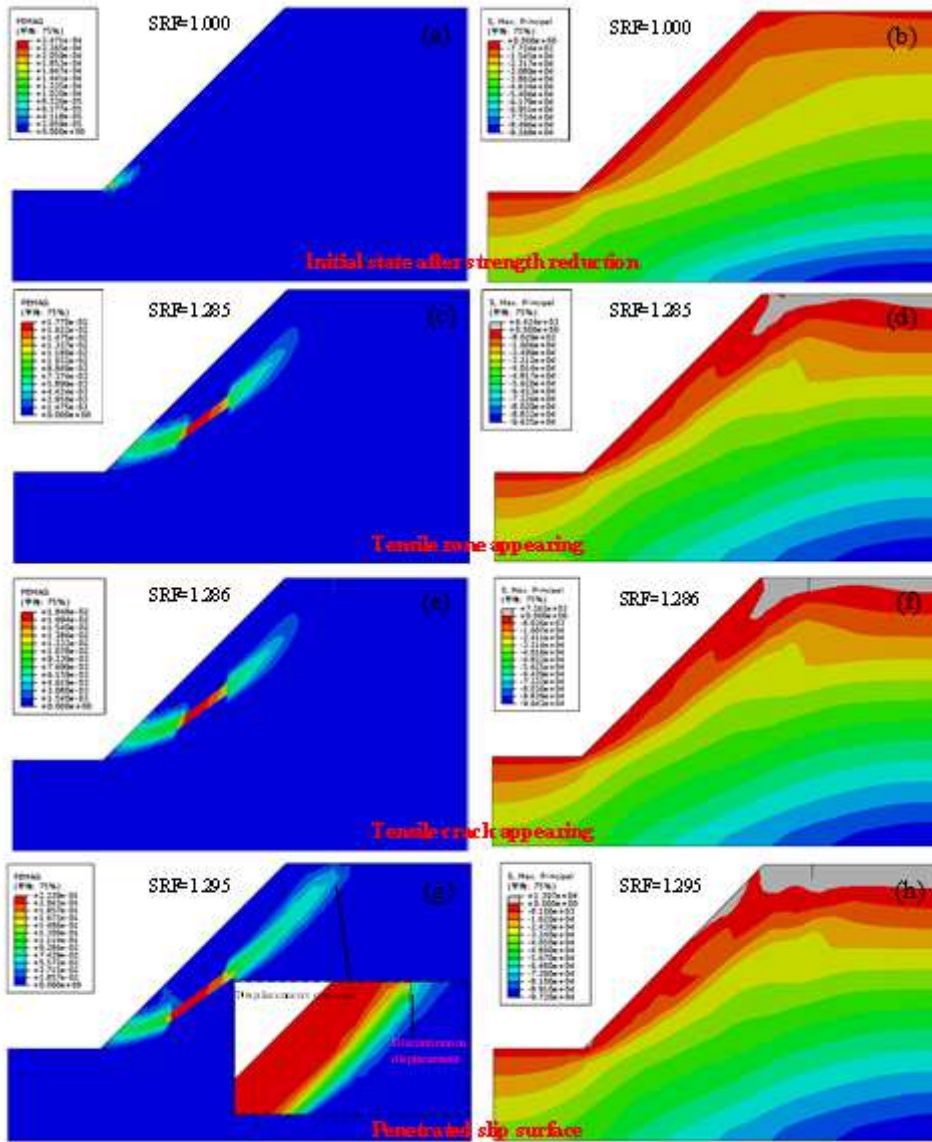


Figure 6

Propagation of a tensile crack in a soil slope failure. (a), (c), (e), and (g) incorporate the contour map of plastic strain magnitude; (b), (d), (f), and (h) incorporate the contour map of maximum principal stress.

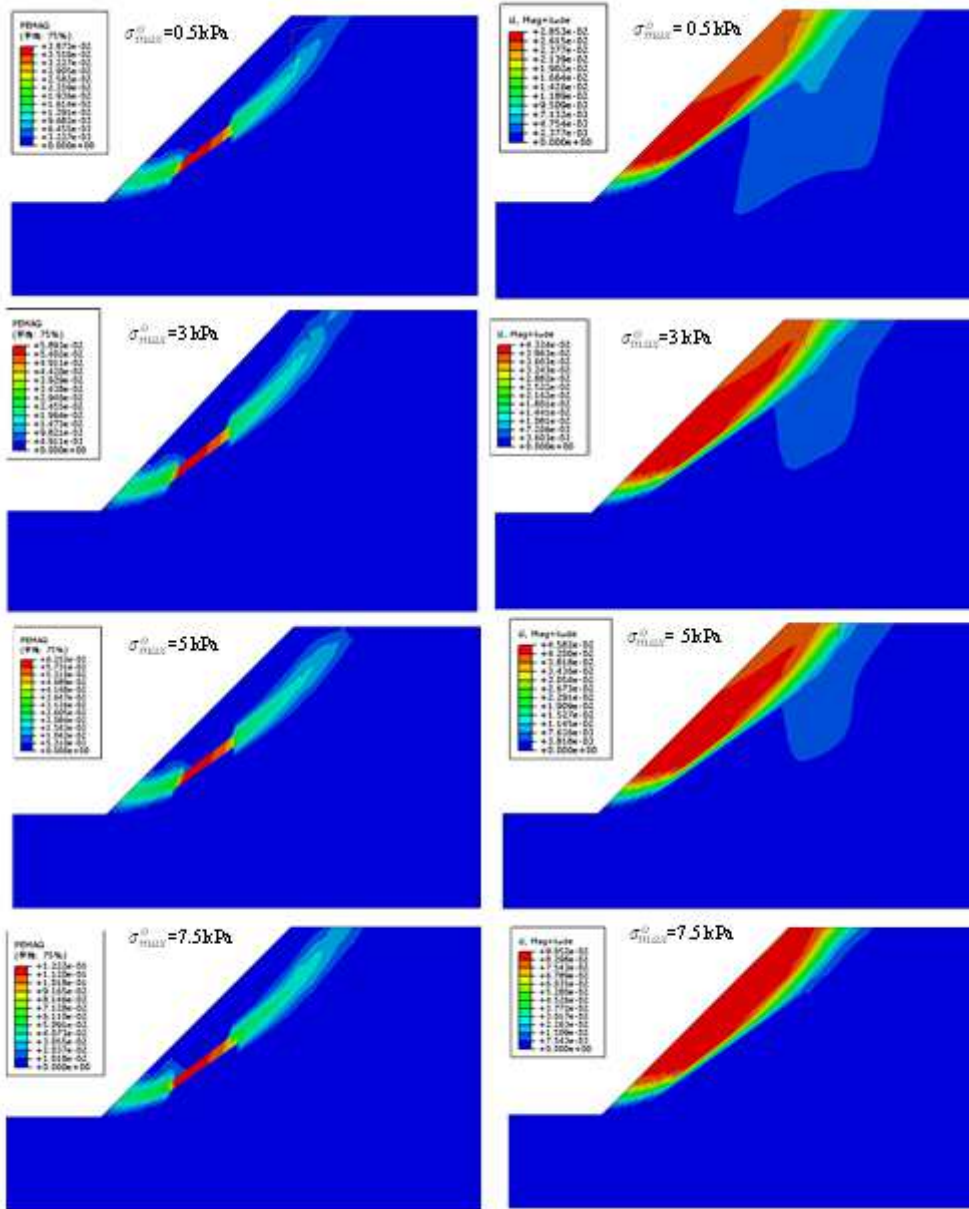


Figure 7

Morphology of tensile crack at the time of a slope failure under different soil damage strengths. (a), (c), (e), and (g) the magnitude of plastic strain; (b), (d), (f), and (h) the magnitude of total displacement.

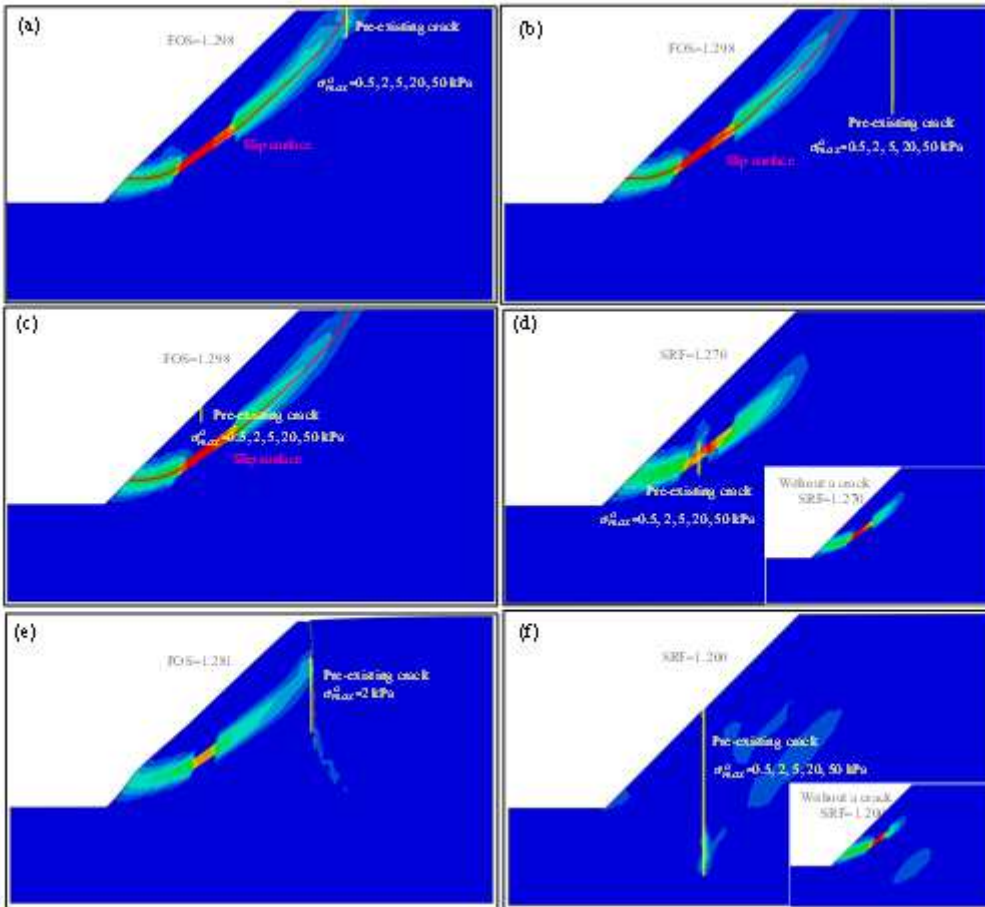


Figure 8

Sensitivity analysis for crack propagation in different conditions based on the contour map of plastic strain magnitude.

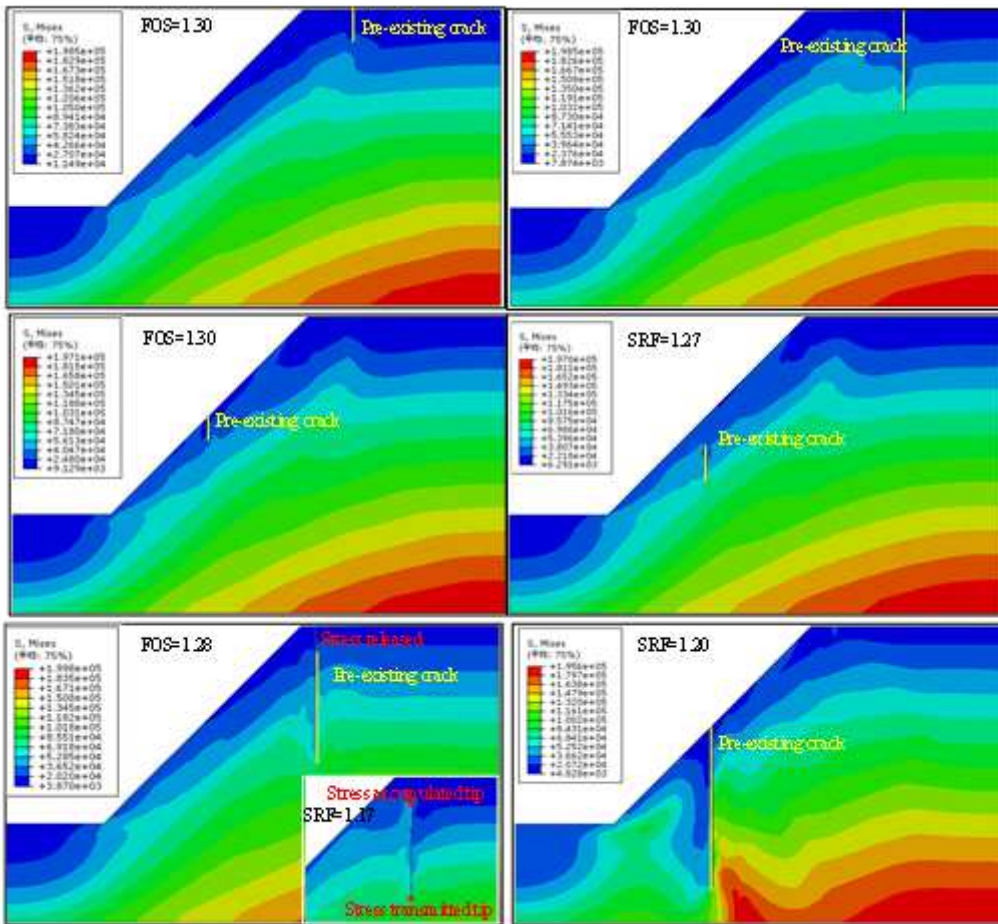


Figure 9

Sensitivity analysis for crack propagation in different conditions based on the contour map of stress magnitude.

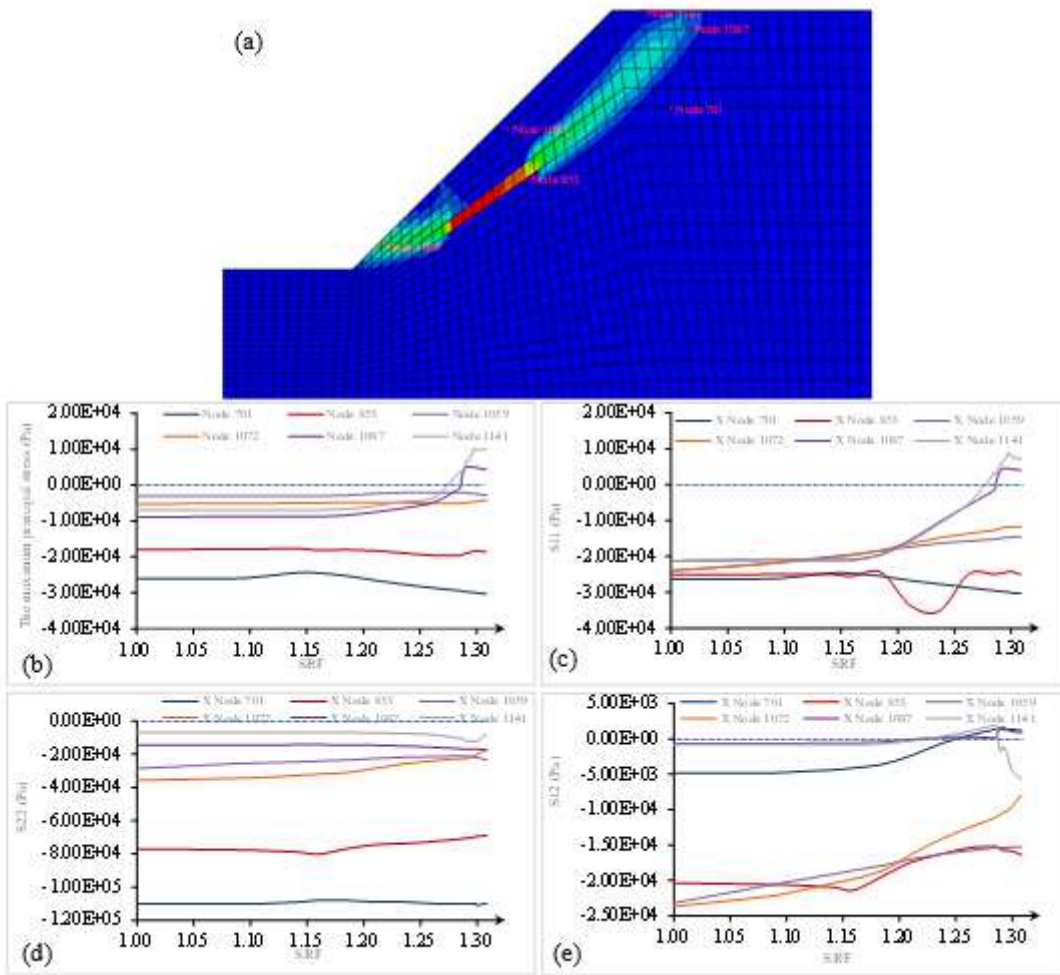


Figure 10

Stress variation at different positions of slope. (a) Monitoring location of the model, (b) maximum principal stress of the monitoring nodes, (c) S11 of the monitoring nodes, (d) S22 of the monitoring nodes, and (e) S12 of the monitoring nodes.